JOURNAL OF SOLID STATE CHEMISTRY **130,** 28–34 (1997)
ARTICLE NO. SC967266

Structure Characterization and Ionic Conductivity of $Ag_2VP_2O_8$

Abdelaali Daidouh, M. L. Veiga, and C. Pico[1]

Depto. Química Inorganica I, Facultad de Ciencias Químicas, Universidad Complutense, 28040 Madrid, Spain

Received July 12, 1996; in revised form December 13, 1996; accepted December 19, 1996

This paper reports the structure, transport properties, and magnetic susceptibility of the new silver vanadium(IV) diphosphate $Ag_2VP_2O_8$. The structure was refined from X-ray powder diffraction by the Rietveld method. This phase, isostructural to $Na_2VP_2O_8$, crystallizes in the monoclinic space group $P2_1/c$ with the parameters $a = 7.739$ Å, $b = 13.611$ Å, $c = 6.294$ Å, $\beta = 99.01^\circ$, $Z = 4$, and $V = 654.8$ Å^3. It consists of $[VP_2O_8]_\infty$ layers, observed in many phosphorus compounds, parallel to the (010) plane interleaved with silver cations. The structure delimits rather large tunnels running along the [010] direction, where silver cations are located too. Electrical transport measurement has been carried out, by complex impedance, to determine the ionic conductivity of the compound and its evolution with temperature and frequency. Curie-type behavior is observed in the magnetic susceptibility which confirms the tetravalent state of vanadium and suggests no magnetic interactions. © 1997 Academic Press

INTRODUCTION

Compounds with structures that contain well-developed layers of atoms and those with tunnel frameworks have been extensively studied, not only because of the rich and complex structural chemistry, but also because the layers may be separated chemically and become the site of interlamellar chemistry. In principle the chemical characteristics of tunnel materials are *a priori* favorable to cation mobility.

On the other hand, the vanadium phosphate oxides have received considerable attention, due to their use as heterogeneous catalysts in various organic reactions (1–5). Some exhibit an extraordinary, rich chemistry owing to the various oxidation states and flexible coordination of vanadium (6–9). In this respect it is interesting to consider the variety of ways in which phosphate tetrahedra and vanadyl octahedra can be interlinked (10).

The vanadyl diphosphates AVP_2O_8 (A = K, Cs, and Rb) (11, 12) are characterized by layer and tunnel structures, where the alkali metal cations are located; $K_2VP_2O_8$ is tetragonal and $Rb_2VP_2O_8$ and $Cs_2VP_2O_8$ are orthorhombic with the space groups $P4mb$, $P2_12_12_1$, and $Pnma$, respectively. Their structures are built up from pure VO_5 pyramids and P_2O_7 groups, but the way in which they are connected is quite different. In other compounds water can be introduced simultaneously with univalent cations as in $Na_5V_2P_3O_{14} \cdot H_2O$ (13). The common feature in the compounds $Na_2VP_2O_8$ (14) and $Ag_2VP_2O_8$ deals with the particular geometry of the VO_6 octahedra which is characterized by a short V–O bond. The objectives of the present work were, first, the determination of the $Ag_2VP_2O_8$ structure by the Rietveld method and, second, the study of temperature variation by ac conductivity, as well as frequency dispersion of the dielectric constant in the frequency range 1 Hz–10 MHz.

[1] To whom correspondence should be addressed.

EXPERIMENTAL

Synthesis

Powder samples of pure $Ag_2VP_2O_8$ were prepared by solid state reaction methods starting from $AgNO_3$, V_2O_4, and $(NH_4)_2HPO_4$ weighed in stoichiometric quantities. First, the starting materials were well mixed, ground in an agate mortar, and heated at 673 K for a time sufficient to complete the evolution of gaseous products (N_2O_3, H_2O, and NH_3). Then they were progressively fired between 773 and 823 K in air for 4 days, with intervening mixing and grinding, until no change was detected by X-ray diffraction.

The final product, which is a green powder, was pressed (5 ton/cm^2) to form pellets 12.5 mm in diameter and 1.4 mm thick and sintered overnight at 823 K. Finally, the pellets were coated with a thin layer of conducting graphite adhesive paint on opposite sides.

X-Ray Diffraction

X-ray powder diffraction patterns were registered at a rate of $0.1^\circ(2\theta)\,\text{min}^{-1}$ using a Philips X'pert MPD, Cu$K\alpha$ radiation, a step scan $0.04^\circ(2\theta)$ between 10 and $120^\circ(2\theta)$, and a counting time of 12 s for each step. Finally, the selected X-ray diffraction profile was analyzed and refined by means of the Rietveld method (15).

0022-4596/97 $25.00
Copyright © 1997 by Academic Press
All rights of reproduction in any form reserved.

Ionic Conductivity

Ac conductivity values of the coated pellet were obtained by the well-known complex impedance method in the temperature range 363–673 K. A frequency resonance analyzer (Solatron 1260) was used for electrical characterization over the frequency range 1 Hz–10 MHz.

Magnetic Measurements

Variable temperature magnetic susceptibility $\chi(T)$ data were obtained by using the Faraday method in the temperature range 70–300 K in the DSM-5 pendule magnetometer on 52.3 mg of the powder.

RESULTS AND DISCUSSION

X-Ray Diffraction

X-ray diffraction results were analyzed by means of the Rietveld method. The program used minimizes the function $\chi^2 = (R_{wp}/R_{exp})^2$. Good agreement between the final observed, calculated, and difference diffraction profiles is seen in Fig. 1. The unit cell parameters and reliability factors are listed in Table 1, final atomic coordinates in Table 2, and bond lengths in Table 3. Due to the lower scattering of oxygen atoms the values for bond distances are not very reliable in these cases, but all of them agree well with the Shannon ionic radii and those reported in the literature for related systems.

TABLE 1
Summary of Structure Parameters (Rietveld Refinement Data)

1. Structure parameters	
Space group	$P2_1/c$
a (Å)	7.739(1)
b (Å)	13.611(1)
c (Å)	6.294(1)
β (°)	99.00(8)
Z	4
V(Å^3)	654.82(8)
2. Structure solution and refinement	
R_P	11.7
R_{WP}	14.4
R_B	6.03
χ^2	3.79
Parameters refined	58
Reflections	1945

Note. $R_P = 100\sum_i(y_i - y_{ci})/\sum_i(y_i)$. $R_{WP} = [100\sum_i(y_i - y_{ci})^2/\sum_i(y_i)^2]$. $R_B = 100\sum_i(I_i - I_{ci})/\sum_i(I_i)$. $\chi^2 = (R_{WP}/R_{exp})^2$.

Structure Description

As shown in the projection view on the **ab** plane (Fig. 2) the structure of this compound is formed by layers parallel to the (010) plane, which can be described as the association of the $[VPO_8]_\infty$ chains running along the [100] direction (Fig. 3), that are built up from opposite corner-sharing VO_6 octahedra and $P(2)O_4$ tetrahedra. Laterally these chains are interconnected in such a way that each VO_6 octahedron of one $[VPO_8]_\infty$ chain shares one corner with one $P(2)O_4$

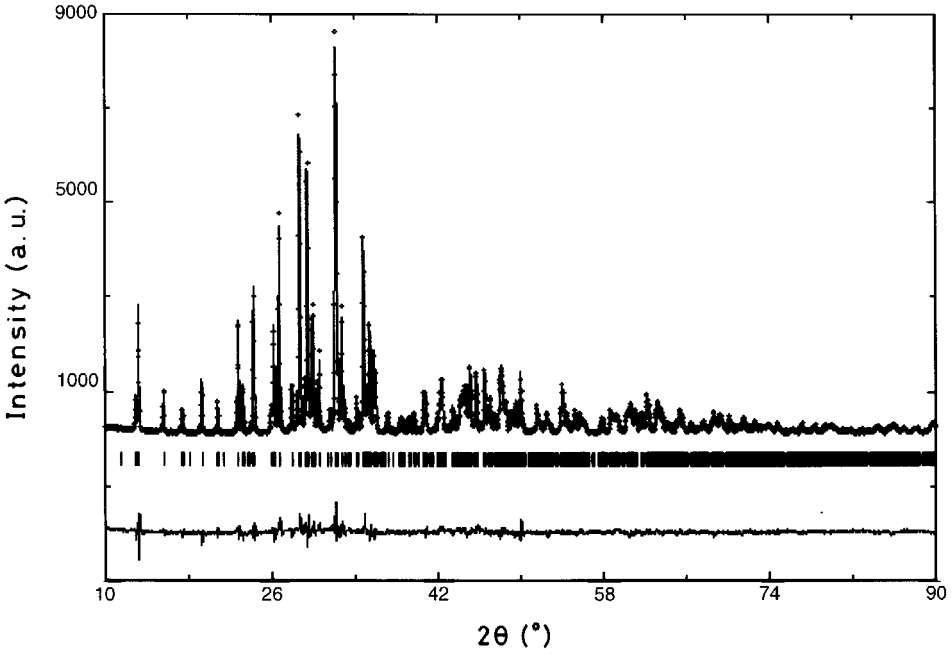

FIG. 1. Observed (. . .) and calculated (—) patterns of $Ag_2VP_2O_8$. The difference pattern is at the same scale.

TABLE 2
$Ag_2VP_2O_8$ Positional Parameters

	x/a	*y/b*	*z/c*
V	0.223(7)	0.422(3)	0.269(3)
P(1)	0.359(9)	0.627(9)	0.538(8)
P(2)	0.171(6)	0.479(5)	0.745(1)
Ag(1)	0.062(4)	0.701(8)	0.150(9)
Ag(2)	0.514(2)	0.353(3)	0.914(2)
O(1)	0.361(3)	0.557(7)	0.358(3)
O(2)	0.466(8)	0.358(4)	0.314(6)
O(3)	0.123(5)	0.324(5)	0.198(5)
O(4)	0.231(6)	0.408(6)	0.586(1)
O(5)	0.015(3)	0.521(8)	0.244(1)
O(6)	0.272(1)	0.454(0)	− 0.032(0)
O(7)	0.221(9)	0.592(7)	0.693(2)
O(8)	0.286(9)	0.726(4)	0.473(5)

Note. All the atoms are located in the general position 4*e* with an occupancy factor of 1.

tetrahedron of the adjacent chain, giving rise to the resulting formula $[V_2P_2O_{14}]_\infty$. Such double chains are observed previously in molybdenum and vanadium phosphates as $Na_3Mo_3P_3O_{16}$ (16) and β-VPO_5 (17).

TABLE 3
Oxygen Atoms Surrounding V^{4+}, P^{5+}, and Ag^+ with Distances (Å) < 3.2 and Sums of Ionic Radii

V–O(1) = 2.157(8)	V–O(4) = 1.994(1)
V–O(2) = 2.051(0)	V–O(5) = 2.093(5)
V–O(3) = 1.569(8)	V–O(6) = 2.035(8)
P(1)–O(1) = 1.485(8)	P(2)–O(4) = 1.514(6)
P(1)–O(2^{i}) = 1.515(7)	P(2)–O(5^{ii}) = 1.458(7)
P(1)–O(7) = 1.625(1)	P(2)–O(6^{iii}) = 1.533(6)
P(1)–O(8) = 1.487(6)	P(2)–O(7) = 1.634(5)
Ag(1)–O(1) = 3.155(2)	Ag(2)–O(1^{i}) = 2.419(7)
Ag(1)–O(3^{iv}) = 2.486(3)	Ag(2)–O(2^{iii}) = 2.603(9)
Ag(1)–O(3^{v}) = 2.459(4)	Ag(2)–O(2^{vii}) = 2.959(5)
Ag(1)–O(5) = 2.558(4)	Ag(2)–O(4) = 2.863(6)
Ag(1)–O(7^{vi}) = 3.052(1)	Ag(2)–O(6^{iii}) = 2.388(0)
Ag(1)–O(8) = 2.479(3)	Ag(2)–O(6^{i}) = 3.127(4)
Ag(1)–O(8^{vi}) = 2.414(5)	Ag(2)–O(7^{viii}) = 3.038(8)
	Ag(2)–O(8^{ix}) = 2.347(7)

	Sums of ionic radii (Å)	Shannon values (Å)
V–O	1.98	1.96
P(1)–O	1.53	1.57
P(2)–O	1.53	1.57
Ag(1)–O	2.66	2.62
Ag(2)–O	2.72	2.68

Note. Symmetry code: (i) $1-x$, $1-y$, $1-z$; (ii) $-x$, $1-y$, $1-z$; (iii) x, y, $1+z$; (iv) $-x$, $1-y$, $-z$; (v) $-x$, $\frac{1}{2}+y$, $\frac{1}{2}-z$; (vi) x, $\frac{3}{2}-y$, $-\frac{1}{2}+z$; (vii) x, $\frac{1}{2}+y$, $\frac{1}{2}+z$; (viii) $1-x$, $1-y$, $2-z$; (ix) $1-x$, $\frac{1}{2}+y$, $\frac{3}{2}-z$.

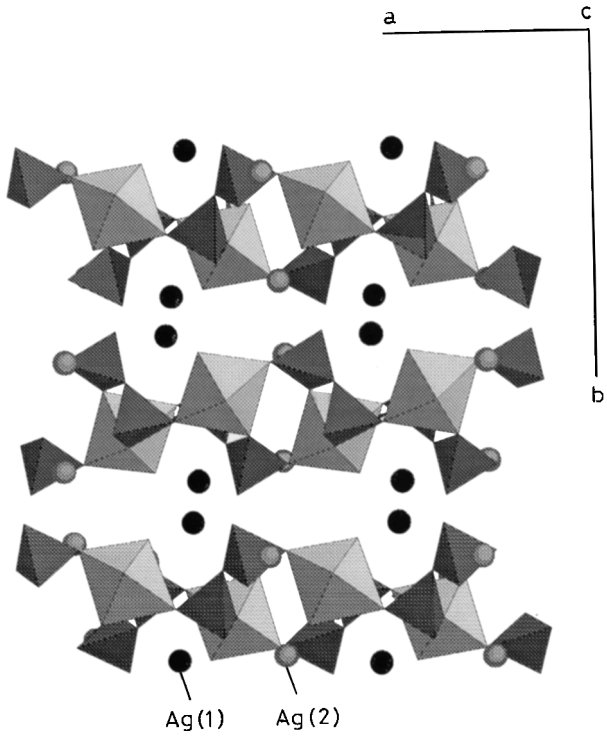

FIG. 2. View of the infinite layers of VO_6 octahedra and PO_4 tetrahedra running along the *c* axis.

The double chains are interconnected, moreover through $P(1)O_4$ tetrahedra forming the $[VP_2O_8]_\infty$ host lattice. In fact, $P(1)O_4$ tetrahedron shares two corners with one VO_6 octahedron of each $[V_2P_2O_{14}]_\infty$ parallel double chain. The third vertex O(7) is shared with $P(1)O_4$ of one $[V_2P_2O_{14}]_\infty$

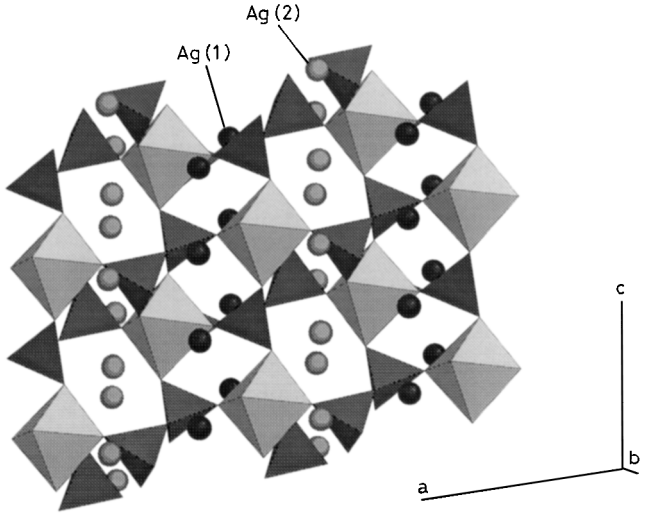

FIG. 3. Projection of the structure along *b* axis. The position of Ag(2) in tunnels are lightly shaded to distinguish them from the darker shaded Ag(1) positions.

double chain exhibiting thus $[VP_2O_{11}]$ units, which built up from one P_2O_7 group sharing two of its apices with the same VO_6 octahedron, the remaining vertex O(8) being free. In the same way, the shorter V–O(3) bond (1.57 Å) corresponds to the free apex of the VO_6 octahedron which can be interpreted as the result of the ability of V(IV) to form a vanadyl group VO.

The fact that each VO_6 octahedron and each P_2O_7 group exhibits one free apex pointed toward the interlayer suggests for this structure great flexibility.

On the other hand, the structure is characterized by a large six-sided window giving rise to large tunnels running along the *b* axis (Fig. 3).

The monovalent cations Ag^+ are on two independent sites: Ag(1), located between the layers (Fig. 2), are sevenfold coordinated (Fig. 4a) whereas Ag(2), in the tunnels (Fig. 3), exhibit an eightfold coordination (Fig. 4b). These cations can migrate and therefore this material could be a good ionic conductor. Such properties are investigated in the present paper.

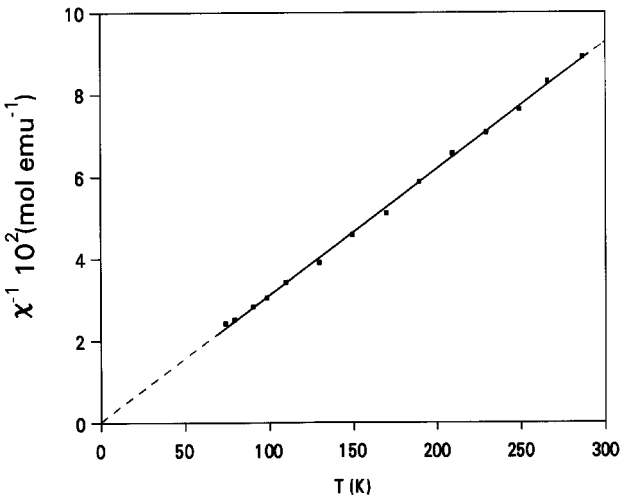

FIG. 5. Plots of inverse magnetic susceptibility, χ^{-1}, versus temperature, T, for a powder sample of $Ag_2VP_2O_8$.

Magnetic Measurements

Magnetic susceptibility was measured and Fig. 5 shows the temperature dependence of the reciprocal molar magnetic susceptibility between 70 and 300 K. It can be observed that $Ag_2VP_2O_8$ obeys a Curie law; from the slope of this straight line running through the origin, one obtains the Curie constant $C = 0.37$ emu K mol^{-1} and an effective magnetic moment $\mu_{eff} = 2.40\ \mu_B$ close to the expected value for four isolated ions ($s = 1/2$) per unit cell with no magnetic interaction, indeed confirming its tetravalent state.

Ionic Conductivity

Most electrical measurements on ionic conductors, including the determination of dc parameters, are carried out by ac techniques using the complex impedance (Z) plots. The reason for this is that contact and interfacial phenomena make it difficult to determine the dc conductivity directly (18).

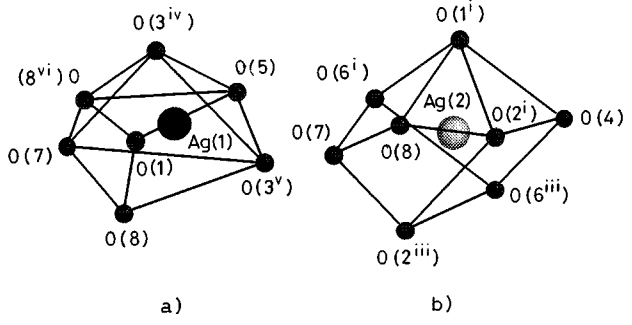

FIG. 4. Coordination polyhedra of (a) Ag(1) atoms and (b) Ag(2) atoms.

To better understand the electrical nature of this solid electrolyte, ac conductivity analysis was used by many researchers (19–21) which includes complex permitivity complex impedance and modulus spectroscopy. These techniques are useful in eliminating the polarization effects and the effect of grain boundaries in the evaluation of the true dc term. Moreover, characteristic properties as relaxation times, carrier hopping rate, and carrier concentration can also be determined (22).

In fact, the behavior may be understood in terms of the frequency dependence of real and imaginary components of the complex permitivity, which may be expressed by the following universal expression, as function of the radian frequency ω (18, 23):

$$\varepsilon(\omega) = (M^*)^{-1} = \varepsilon'(\omega) - j\varepsilon''(\omega) = \varepsilon_\infty + a(j\omega)^{n-1} \quad [1]$$

$$= \varepsilon_\infty + a[\sin(n\pi/2) - j\cos(n\pi/2)]\omega^{n-1}. \quad [2]$$

ε_∞ is the limiting "high frequency" value of the permitivity and the exponent typically falls in the range $0 < n < 1$. The a constant determines the "strength" of the polarizability arising for the universal mechanism in question.

Figures 6a and 6b show the data for $\varepsilon'(\omega)$ and $\varepsilon''(\omega)$ in which we can see very clearly the strong low-frequency dispersion and the very high values attained for the permitivity. In fact, the real part is proportional to $\omega^{-(n-1)}$ for low frequency values (24). This behavior is characteristic of the interaction between mobile cations occupying neighboring sites in the tunnels or in the interlayers, where the conduction takes place.

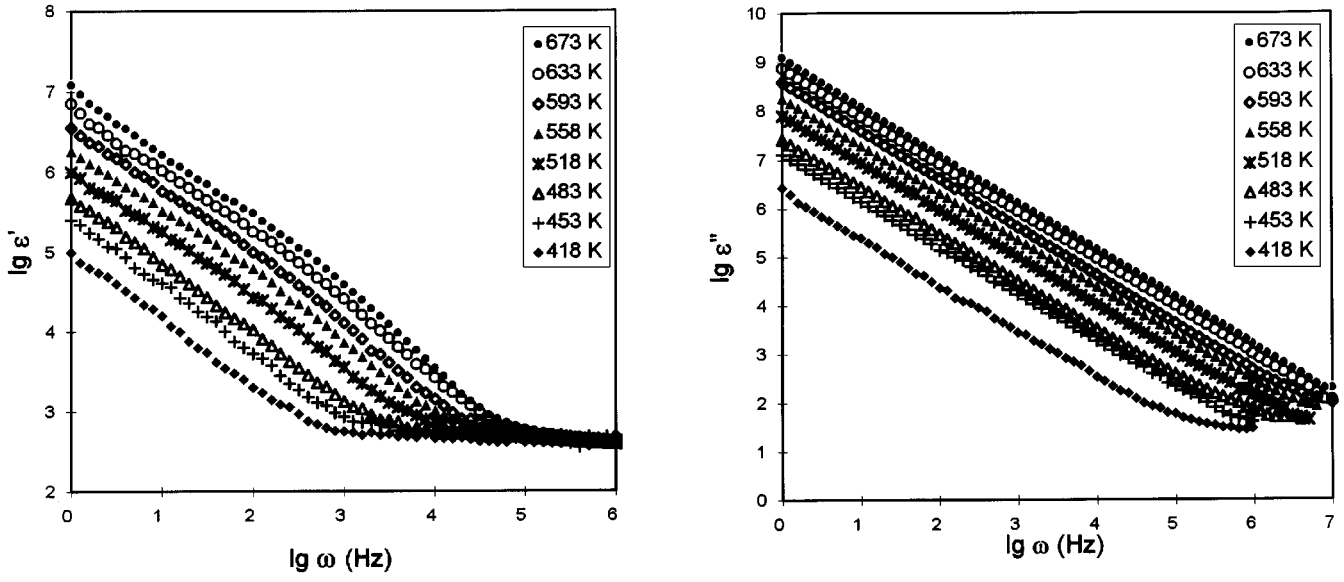

FIG. 6. (a) $\log \varepsilon'$ and (b) $\log \varepsilon''$ versus $\log \omega$ at different temperatures.

The $\varepsilon''(\omega)$ response is dominated by a true dc conduction mechanism as deduced from the -1 slop in the $\varepsilon''(\omega)$ graph at all temperature.

In Fig. 7 typical plots of ac conductivity are depicted. The curves show a frequency-independent plateau corresponding to dc conductivities. It is noteworthy that electrode polarization effects lead to a low-frequency dispersion. However, at higher frequencies the conductivity dispersion follows the power-law dependence, as observed in many hopping ion conductors (25). Generally, through (26), the experimental data points were fitted to a single power-law of the form $\sigma(\omega) = \sigma(0) + A\omega^n$, where $\sigma(0)$ corresponds to a frequency-independent plateau and the latter is usually identified with the dc term. A is a temperature-dependent parameter and n is a slope of high-frequency dispersion data assuming values between 0 and 1.

A thermally activated term ω_p [$\omega_p = \{\sigma(0)/A\}^{1/n}$], which is proportional to the ion hopping rate (27), can be found by inspection of the ac data since $\omega_p = \omega$ when $\sigma(\omega) = 2\sigma(0)$. In Fig. 6 the arrows indicate the attempt frequency ω_p.

Normalized complex modulus spectra (22), M''/M''_{max} ($M'' = j\omega C_0 Z^* = M' + jM''$, C_0 refers to the vacuum capacitance of the cell), vs log frequency are given in Fig. 8

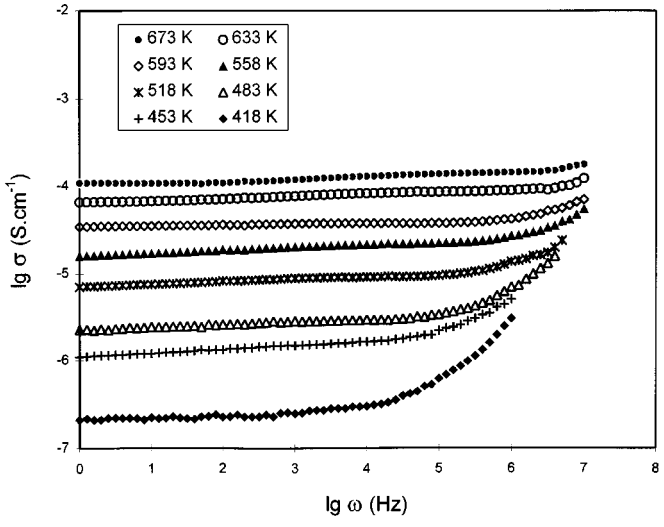

FIG. 7. Plots of log of conductivity versus log of frequency at different temperatures.

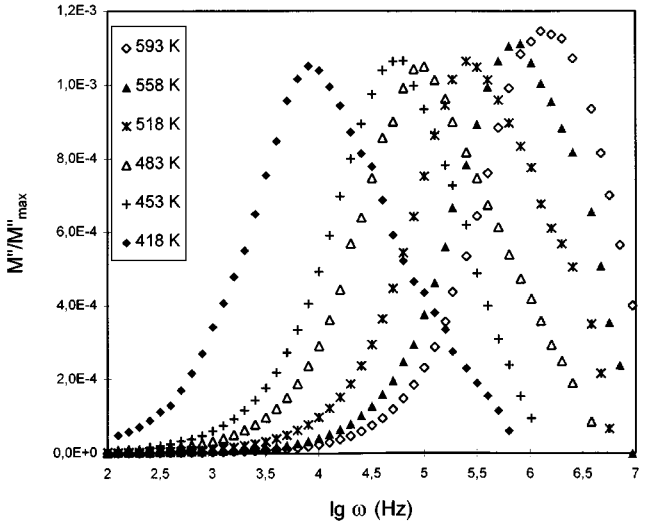

FIG. 8. Normalized modulus (M'') spectra at various temperatures.

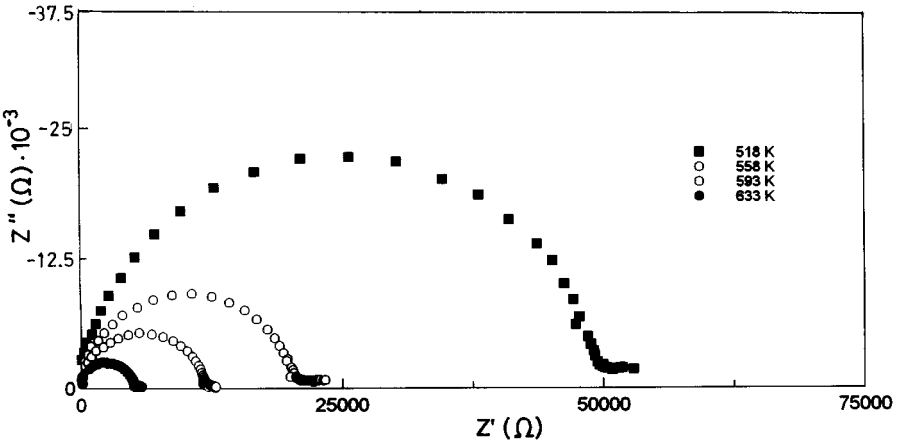

FIG. 9. Complex impedance plots for $Ag_2VP_2O_8$ powder at various temperatures.

at various temperatures. Such a graph shows that the asymmetric peak shifts with change in temperature, as expected, and also that this material is not an ideal electrolyte since the peak spectra are broader than the Debye spectra. This fact corresponds to an ideal solid electrolyte represented by a single parallel RC element.

Indeed, broader peaks can be assigned to the summation of the distribution of relaxation times ($\tau_\sigma = 1/F_p$), calculated from the peak frequency, F_p (Fig. 8), occurring within the bulk material (as opposed to interfacial or intergranular effects).

Figure 9 shows examples of complex impedance plots. Conductivity was estimated from the values of the intersection of an extrapolated semicircle and the real axis (28).

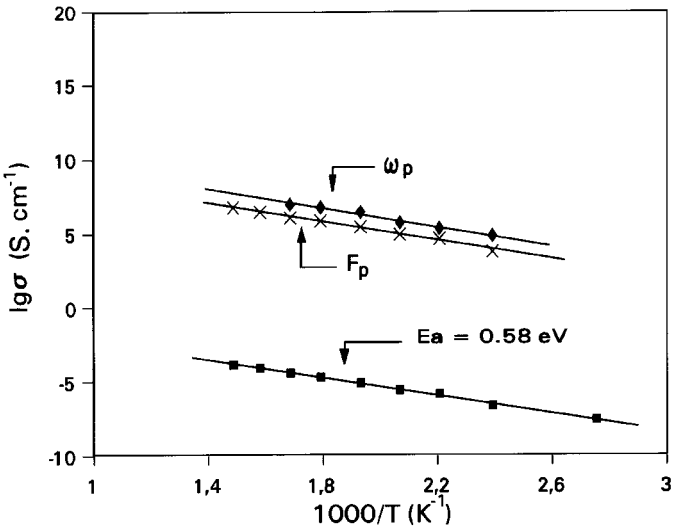

FIG. 10. Temperature dependence of conductivity, σ, inverse relaxation times, ($\tau^{-1} = F_p$), and the attempt frequency, ω_p.

Ionic conductivity values determined from the (Z) diagrams were analyzed by an Arrhenius equation of the form $\sigma = \sigma_0 \exp(-E_a/KT)$, were σ_0 and E_a represent the pre-exponential factor and activation energy, respectively, with K and T taking the usual meanings. Figure 10 illustrates the linear plots of $\log\sigma$ vs $1000/T$. The activation energy deduced from the slope was $E_a = 0.58$ eV. The σ values at 558 and 673 K were $\sigma_{558} = 2.08 \times 10^{-5}\,\Omega^{-1}\,cm^{-1}$ and $\sigma_{673} = 1.43 \times 10^{-3}\,\Omega^{-1}\,cm^{-1}$.

The peak frequency terms, F_p, and those of ω_p are represented with the Arrhenius plots of $\log\sigma$ vs $1000/T$ for comparison (Fig. 10). The parallel lines indicate that F_p and ω_p are thermally activated and that they bear the same activation energy as σ. This fact explains that the conductivity dispersion, as discussed before, was not due to any localized dielectric loss or to the electrode or interfacial polarization (29), but it can be attributed to the hopping motion of the mobile Ag ions.

ACKNOWLEDGMENTS

We are indebted to the DGICYT (PB 92-0124) and CICYT (MAT 94-0729) for financial support.

REFERENCES

1. P. T. Nguyen and A. W. Sleight, *J. Solid State Chem.* **122,** 259 (1996).
2. J. W. Johnson, D. C. Johnston, A. J. Jacobson, and J. R. Brody, *J. Am. Chem. Soc.* **106,** 8123 (1984).
3. T. Kanazawa, "Inorganic Phospate Materials." Elsevier, Amsterdam, 1991.
4. A. W. Sleight, *Catal. Today* **1,** 347 (1987).
5. B. K. Hodentt, *Catal. Rev. Sci. Eng.* **27,** 373 (1985).
6. A. Grandin, A. Leclaire, M. M. Borel, and B. Raveau, *J. Solid State Chem.* **115,** 521 (1995).
7. R. C. Hanshalter, Z. Wang, M. E. Thompson, J. Zubieta, and Charles J. O'Connor, *J. Solid State Chem.* **108,** 259 (1994).

8. A. Leclaire, J. Chardon, A. Grandin, M. M. Borel, and B. Raveau, *J. Solid State Chem.* **108,** 291 (1994).
9. C. Ninclaus, R. Retoux, D. Rioux, and G. Férey, *J. Solid State Chem.* **122,** 139 (1996).
10. A. Leclaire, H. Chahboun, D. Goult, and B. Raveau, *J. Solid State Chem.* **77,** 170 (1988).
11. YU. E. Gorbonova, S. A. Linde, A. V. Lavrov, and Y. V. Tananev, *Dokl. Akad. Nauk SSSR.* **250**(2), 350 (1980).
12. K. H. Lii and S. L. Wang, *J. Solid State Chem.* **82,** 239 (1989).
13. L. Benhamada, A. Grandin, M. M. Borel, A. Leclaire, and B. Raveau, *J. Solid State Chem.* **96,** 390 (1992).
14. L. Benhamada, A. Grandin, M. M. Borel, A. Leclaire, and B. Raveau, *J. Solid State Chem.* **101,** 154 (1992).
15. J. Rodriguez-Carvajal, "Fullprof Program. III" Grenoble, France, 1993.
16. G. Constentin, M. M. Borel, A. Grandin, A. Borel, and B. Raveau, *J. Solid State Chem.* **79,** 99 (1991).
17. R. Gopal and C. Calvo, *J. Solid State Chem.* **5,** 432 (1972).
18. A. K. Jonscher, *J. Mater. Sci.* **13,** 553 (1978).
19. D. P. Almond, G. K. Duncan, and A. R. West, *J. Solid State Ionics* **8,** 159 (1983).
20. I. D. Raistrick, *J. Solid State Ionics* **18/19,** 40 (1986).
21. J. Isasi, M. L. López, M. L. Veiga, E. Ruiz-Hitzky, and C. Pico, *J. Solid State Chem.* **116** (1995).
22. B. V. R. Chowdari, K. Radhakrishan, K. A. Thomas, and G. V. Subba Rao, *Mater. Res. Bull.* **24,** 221 (1989).
23. A. K. Jonscher, K. L. Deori, J. M. Reau, and J. Moali, *J. Mater. Sci.* **14,** 1308 (1979).
24. A. K. Jonscher, "Dielectric Relaxation in Solids." Chelsea Dielectric Press, London, 1983.
25. A. K. Jonscher, *Nature* **264,** 673 (1977).
26. R. M. Hill and A. K. Jonscher, *J. Non-Cryst. Solids* **32,** 53 (1979).
27. D. P. Almond, C. C. Hunter, and A. R. West, *J. Mater. Sci.* **19,** 3236 (1984).
28. H. Yamane, S. Kikkawa, and M. Koisumi, *J. Solid State Chem.* **71,** 1 (1987).
29. R. J. Grant, Y. M. Hodge, M. D. Ingram, and A. R. West, *J. Am. Ceram. Soc.* **60,** 226 (1977).